Modeling the effect of small-scale magnetic turbulence on the X-ray properties of Pulsar Wind Nebulae

N. Bucciantini,[1,2,3]* R. Bandiera,[1] B. Olmi[1,2,3] and L. Del Zanna[1,2,3]

[1]*INAF - Osservatorio Astrofisico di Arcetri, Largo E. Fermi 5, I-50125 Firenze, Italy*
[2]*Dipartimento di Fisica e Astronomia, Università degli Studi di Firenze, Via G. Sansone 1, I-50019 Sesto F. no (Firenze), Italy*
[3]*INFN - Sezione di Firenze, Via G. Sansone 1, I-50019 Sesto F. no (Firenze), Italy*

ABSTRACT

Pulsar Wind Nebulae (PWNe) constitute an ideal astrophysical environment to test our current understanding of relativistic plasma processes. It is well known that magnetic fields play a crucial role in their dynamics and emission properties. At present, one of the main issues concerns the level of magnetic turbulence present in these systems, which in the absence of space resolved X-ray polarization measures cannot be directly constrained. In this work, we investigate, for the first time using simulated synchrotron maps, the effect of a small-scale fluctuating component of the magnetic field on the emission properties in X-ray. We illustrate how to include the effects of a turbulent component in standard emission models for PWNe and which consequences are expected in terms of net emissivity and depolarization, showing that the X-ray surface brightness maps can provide already some rough constraints. We then apply our analysis to the Crab and Vela nebulae and by comparing our model with *Chandra* and Vela data, we found that the typical energies in the turbulent component of the magnetic field are about 1.5–3 times the one in the ordered field.

Key words: MHD – polarization – radiation mechanisms: non-thermal – relativistic processes – ISM: individual objects: Crab nebula – ISM: supernova remnants.

1 INTRODUCTION

Pulsar Wind Nebulae (PWNe) are bubbles of relativistic particles and a magnetic field arising from the interaction of the relativistic pulsar wind with the ambient medium (interstellar medium [ISM] or supernova remnant). They shine in non-thermal (synchrotron and inverse Compton) radiation in a broad range of frequencies from radio wavelengths to γ-rays (see Gaensler & Slane 2006 for a review). At X-rays, many PWNe show an axisymmetric feature known as *jet-torus structure*. This feature has by now been observed in a number of PWNe among which are the Crab nebula (Weisskopf et al. 2000), Vela (Helfand, Gotthelf & Halpern 2001; Pavlov et al. 2001) and MSH 15-52 (Gaensler et al. 2002; DeLaney et al. 2006), to name just a few. It is now commonly accepted that this structure arises due to the interplay of the anisotropic energy flux in the wind with the toroidal magnetic field, as confirmed by a long series of numerical simulations (Komissarov & Lyubarsky 2003, 2004; Del Zanna, Amato & Bucciantini 2004; Del Zanna et al. 2006; Volpi et al. 2007; Camus et al. 2009; Porth, Komissarov & Keppens 2014; Olmi et al. 2014, 2016). In general, two-dimensional models are built on the axisymmetric assumption of a purely toroidal magnetic field, while three-dimensional models usually have a much lower resolution and

can only investigate large-scale deviations from axisymmetry. However, recently, several arguments have been put forward advocating the presence of small-scale turbulence in PWNe: the presence of a large diffuse X-ray halo at distances in excess of the naive expectation for synchrotron cooling and advection (Tang & Chevalier 2012; Bühler & Blandford 2014; Zrake & Arons 2016); the suggestion that radio-emitting particles could be continuously re-accelerated in the body of the nebula (Olmi et al. 2015; Tanaka & Asano 2016); and the observation of recurrent γ-ray flares requiring localized strong current sheets (Uzdensky, Cerutti & Begelman 2011).

Radio polarization maps are available, but being radio emission dominated by the outer region of PWNe, where the effects of the interaction with the SNR are stronger, they provide at best a good estimate of the degree of ordered versus disordered magnetic field for the overall nebula, but cannot be used to constrain the conditions in the region close to the termination shock where most of the variability and the acceleration processes take place. In the Crab nebula, the polarized fraction in radio is on average ∼16 per cent (Conway 1971; Ferguson 1973; Velusamy 1985; Aumont et al. 2010) with peaks up to 30 per cent, lower than in optical, where the average polarized fraction is ∼25 per cent (Velusamy 1985). Moreover the polarized flux in radio anticorrelates with the location of the X-ray torus. The values of the radio polarization are consistent with a largely turbulent magnetic field in the outer part of the nebula (Bucciantini et al., in preparation).

* E-mail: niccolo@arcetri.astro.it

Recently, high-resolution HST observations in polarized light have been presented both for the inner region of the Crab nebula (Moran et al. 2013) and for the Vela PWN (Moran, Mignani & Shearer 2014). The study of the Crab nebula focused on the brightest optical features, namely the *knot* and the *wisps*, which are shown to have typical polarized fractions of about 60 per cent and 40 per cent, respectively. The results in the Crab nebula are consistent with the general picture of a strongly ordered toroidal magnetic field just downstream of the termination shock with a possible hint of the development of turbulence: the polarized fraction of the wisps is lower than the one in the knot and numerical simulations suggest the former to be slightly more downstream than the latter. Vela is not detected in polarized optical light, but this might not be very constraining given that there is no optical counterpart observed for this nebula (Marubini et al. 2015). The major problem with optical emission is that there is usually a large foreground, often polarized (see for example the polarization analysis of the Crab nebula presented in Hester 2008), and the jet-torus structure, which is so prominent in X-ray, is much fainter. Ideally, one would like to probe these systems using X-ray polarimetry (Bucciantini 2010) and there is a large interest in the scientific community for such an objective (Soffitta et al. 2013; Weisskopf et al. 2016). Incidentally, the Crab nebula is, at the moment, the only object with a polarization detected in X-ray (Weisskopf et al. 1978).

In the past years, several models have been presented to simulate the X-ray emission map of PWNe (with a particular focus on Crab), ranging from simplified toy-models (Ng & Romani 2004; Schweizer et al. 2013) to more complex multidimensional time-dependent simulations (Volpi et al. 2007; Porth et al. 2014; Olmi et al. 2016). Starting from the early work of Bucciantini et al. (2005), polarization has also been modelled using, in general, a magnetic field geometry derived from numerical simulations (Del Zanna et al. 2006; Porth et al. 2014). However, the presence of small-scale turbulence and its effects, both on the polarized fraction and on the emissivity pattern, have never been taken into account before.

Here we present synthetic polarization maps of PWNe, taking into account the presence of small-scale magnetic turbulence at a subgrid level. In Section 2, we illustrate how the recipe for total and polarized emission can be corrected to take into account magnetic turbulence. In Section 3, using a simple toy model, we show how the effects of turbulence manifest in the intensity map and are thus in principle already accessible from X-ray imaging. In Section 4, we present a semi-analytical model for a thin-ring that allows us to derive simple formulae showing the typical degeneracy between Doppler boosting and turbulence. In Section 5, we apply our results to the Crab and Vela PWNe, objects that have been considered as primary targets for future X-ray polarimetric observations (Weisskopf et al. 2016).

2 POLARIZATION RECIPES AND SUBGRID MODEL

Let us begin by recalling the general recipe to compute the synchrotron intensity and polarization properties, taking into account relativistic Doppler boosting effects, in the case of a fully ordered (at least on the scale of the fluid element under consideration) magnetic field. A complete derivation can be found in Del Zanna et al. (2006). For electrons having a power-law distribution

$$n(\epsilon) = K\epsilon^{-(2\alpha+1)}, \tag{1}$$

where ϵ is the energy in units $m_e c^2$ and belonging to a fluid element with comoving magnetic field $\boldsymbol{B}'$ and velocity with respect

to the observer $\mathbf{v} = \boldsymbol{\beta}c$ (corresponding to a Lorentz factor γ), the emissivity towards the observer at frequency ν is:

$$j(\nu, \boldsymbol{n}) = C \mid \boldsymbol{B}' \times \boldsymbol{n}' \mid^{\alpha+1} D^{\alpha+2}\nu^{-\alpha}, \tag{2}$$

where C is given by synchrotron theory

$$C = \frac{\sqrt{3}}{4}\frac{\alpha+5/3}{\alpha+1}\Gamma\left(\frac{\alpha+5/3}{2}\right)\Gamma\left(\frac{\alpha+1/3}{2}\right)$$
$$\times \frac{e^3}{mc^2}\left(\frac{3e}{2\pi mc}\right)^{\alpha} K, \tag{3}$$

$\boldsymbol{n}'$ is the direction of the observer measured in the comoving frame, related to the one measured in the observer frame $\boldsymbol{n}$ by

$$\boldsymbol{n}' = D\left[\boldsymbol{n} + \left(\frac{\gamma^2}{\gamma+1}\boldsymbol{\beta}\cdot\boldsymbol{n} - \gamma\right)\boldsymbol{\beta}\right], \tag{4}$$

D is the Doppler boosting factor

$$D = \frac{1}{\gamma(1 - \boldsymbol{\beta}\cdot\boldsymbol{n})} \tag{5}$$

and the comoving magnetic field can be computed from the one measured in the observer frame as

$$\boldsymbol{B}' = \frac{1}{\gamma}\left[\boldsymbol{B} + \frac{\gamma^2}{\gamma+1}(\boldsymbol{\beta}\cdot\boldsymbol{B})\boldsymbol{\beta}\right], \tag{6}$$

giving

$$\mid \boldsymbol{B}' \times \boldsymbol{n}' \mid = \frac{1}{\gamma}\sqrt{B^2 - D^2(\boldsymbol{B}\cdot\boldsymbol{n})^2 + 2\gamma D(\boldsymbol{B}\cdot\boldsymbol{n})(\boldsymbol{B}\cdot\boldsymbol{\beta})}. \tag{7}$$

Let us consider a Cartesian observer's reference frame in which X lies along the line of sight $\boldsymbol{n}$ and Y and Z are in the plane of the sky. At this point, it is possible to compute the maps of the various Stokes parameters integrating the contribution of each fluid element along the line of sight through the nebula, according to

$$I(\nu, Y, Z) = \int_{-\infty}^{\infty} j(\nu, X, Y, Z)\,\mathrm{d}X, \tag{8}$$

$$Q(\nu, Y, Z) = \frac{\alpha+1}{\alpha+5/3}\int_{-\infty}^{\infty} j(\nu, X, Y, Z)\cos 2\chi\,\mathrm{d}X, \tag{9}$$

$$U(\nu, Y, Z) = \frac{\alpha+1}{\alpha+5/3}\int_{-\infty}^{\infty} j(\nu, X, Y, Z)\sin 2\chi\,\mathrm{d}X, \tag{10}$$

where the local polarization position angle χ is the angle of the emitted electric field vector $\boldsymbol{e}$ in the plane of the sky. This electric field is related to the one measured at emission in the comoving frame $\boldsymbol{e}'$ by

$$\boldsymbol{e} = \gamma\left[\boldsymbol{e}' - \frac{\gamma}{\gamma+1}(\boldsymbol{\beta}\cdot\boldsymbol{e}')\boldsymbol{\beta} - \boldsymbol{\beta}\times(\boldsymbol{n}'\times\boldsymbol{e}')\right]. \tag{11}$$

In an ideal MHD, it is possible to introduce an auxiliary vector $\boldsymbol{q}$ defined as

$$q_Y = (1 - \beta_X)B_Y + \beta_Y B_X, \quad q_Z = (1 - \beta_X)B_Z + \beta_Z B_X, \tag{12}$$

such that

$$\cos 2\chi = \frac{q_Y^2 - q_Z^2}{q_Y^2 + q_Z^2}, \quad \sin 2\chi = -\frac{2q_Y q_Z}{q_Y^2 + q_Z^2}. \tag{13}$$

In a recent paper, Bandiera & Petruk (2016) have shown that the effect of the small-scale magnetic field fluctuations on the total and the polarized emissivity can be computed analytically, considering a fluid element with a net average field and assuming that

the small-scale fluctuations can be described by an isotropic random Gaussian field with variance $(B'\sigma)^2$ in each direction. The emission is computed considering the electrons to be distributed in the nebula with a power-law distribution function, as specified in equation (1). The variance is just a measure of the ratio of the energy δE in the small-scale fluctuating components over the energy E in the ordered component of the comoving magnetic field: $\delta E/E = 3\sigma^2$. These small-scale fluctuations contribute to the total emissivity, which rises linearly with the energy in the fluctuating components (as long as this energy is smaller than the one associated with the net average magnetic field). They, however, contribute much less to the polarized intensity because of the assumption that they are randomly distributed in orientation. The net effect is to reduce the polarized fraction. Interestingly, the depolarization is almost insensitive to the value of α. One can introduce two correction coefficients defined as

$$\xi(\alpha, B_\perp, \sigma) = \Gamma\left(\frac{3+\alpha}{2}\right) {}_1F_1\left(-\frac{1+\alpha}{2}, 1, -\frac{B_\perp^2}{2B'^2\sigma^2}\right)$$
$$\times \left(\frac{B_\perp}{\sqrt{2}B'\sigma}\right)^{-(1+\alpha)} \quad (14)$$

$$\zeta(\alpha, B_\perp, \sigma) = \frac{1}{2}\Gamma\left(\frac{5+\alpha}{2}\right) {}_1F_1\left(\frac{1-\alpha}{2}, 3, -\frac{B_\perp^2}{2B'^2\sigma^2}\right)$$
$$\times \left(\frac{B_\perp}{\sqrt{2}B'\sigma}\right)^{(1-\alpha)}, \quad (15)$$

where ${}_1F_1(a, b, x)$ is the Kummer confluent hypergeometric function and $B_\perp = |\, \boldsymbol{B}' \times \boldsymbol{n}'\,|$ is the component of the average comoving magnetic field perpendicular to the direction of emission that can be taken from a large-scale simulation or a toy model, leaving only σ as a free parameter.

Then one can compute maps corrected for small-scale fluctuations as

$$I(\nu, Y, Z) = \int_{-\infty}^{\infty} \xi(\alpha, B'_\perp, \sigma) j(\nu, X, Y, Z)\, \mathrm{d}X \quad (16)$$

$$Q(\nu, Y, Z) = \frac{\alpha+1}{\alpha+5/3} \int_{-\infty}^{\infty} \zeta(\alpha, B'_\perp, \sigma) j(\nu, X, Y, Z) \cos 2\chi\, \mathrm{d}X \quad (17)$$

$$U(\nu, Y, Z) = \frac{\alpha+1}{\alpha+5/3} \int_{-\infty}^{\infty} \zeta(\alpha, B'_\perp, \sigma) j(\nu, X, Y, Z) \sin 2\chi\, \mathrm{d}X. \quad (18)$$

It can be shown that it is not correct to model a fluctuating component just by adding a constant unpolarized emission on top of the one derived assuming a totally ordered field. A cautionary remark is here in order: the corrections derived by Bandiera & Petruk (2016) are formally valid only in the limit $\beta \to 0$ when the isotropic assumption in the comoving frame corresponds to the isotropic assumption in the observer's frame. In case of strongly relativistic motions this is in general not true. The correction coefficients in such a case are defined properly in the comoving frame and one would need to perform a Lorentz transformation of the polarization tensor to get the correct result in the observer's reference frame. However, the typical bulk flow in the body of PWNe (and in particular in the torus region) has a speed of $\beta \lesssim 0.5$, leading to differences between the comoving and observer's magnetic field of the order of few per cent at most, as can be seen from equation (6), well below

the level of the quantitative accuracy with which simulated maps can reproduce observations.

3 EMISSION MAPS

In order to show how the presence of small-scale fluctuations of the magnetic field affects the emission pattern of rings and tori, we begin using a simple toy model analogous to the one used in Bucciantini et al. (2005), which serves as a reference for the case of purely ordered magnetic field. Let us just recall here its key parameters. The emission is concentrated in a homogeneously radiating torus around the pulsar. In a spherical reference system (r, θ, ϕ) centred on the pulsar position, this is equivalent to the assumption that

$$K|B'|^{\alpha+1} = \begin{cases} \text{const} & \text{for } (r\sin\theta - R_1)^2 + (r\cos\theta)^2 \leq R_2^2, \\ 0 & \text{otherwise} \end{cases}$$
$$(19)$$

where R_1 is the torus principal radius and R_2 is the radius of the cross-section (in our model we have adopted the ratio $R_1/R_2 = 2.5$). The magnetic field is taken to be purely toroidal, whereas the flow velocity is constant and purely radial. To take into account Doppler boosting effects, we assume a flow speed with $\beta = 0.4$, typical of the values inferred in the torus of Crab nebula and other PWNe (Del Zanna et al. 2004) and a spectral index $\alpha = 0.6$ typical of the brightest X-ray regions in Crab nebula (Mori et al. 2004).

In Fig. 1, we show the results for various values of the amplitude of the fluctuating part σ, in the case of a torus with a symmetry axis inclined by $30°$ on the plane of the sky (for reference to a purely ordered case, consider the upper-right panel of fig. 1 in Bucciantini et al. 2005). It is immediately evident that for $\sigma > 1/\sqrt{3}$, corresponding to a case where the fluctuating components contain the same magnetic energy of the ordered one, the intensity along the torus changes appreciably with respect to the ordered case: as the energy in the fluctuating components rises, the difference in the intensity between the centre of the torus and the sides drops. However, as shown by Bucciantini et al. (2005), the angular sideways trend of the luminosity along the torus is also strongly affected by Doppler boosting, so in principle one can obtain similar trends lowering the flow speed (see Section 4). Interestingly, it can be shown that for a flow speed with $\beta \lesssim 0.5$, the two effects can be disentangled looking also at the brightness difference between the front and back sides of the torus. Such brightness difference is insensitive to the value of σ and depends only on β (see the Appendix), so it can be used to set a lower limit to the flow speed (see again fig. 1 of Bucciantini et al. 2005). On the other hand, the presence of a fluctuating component is very effective in raising the luminosity at the sides of the torus, thus the brightness difference between the front and sides can be used to get another constraint and set limits on σ. Interestingly, as shown in Fig. 1, maps in polarized intensity show little or no variation at all in their pattern for any value of σ, what changes is the polarized intensity (the polarized fraction). This can be easily understood recalling that in our subgrid model the effect of small-scale fluctuations on the polarized intensity is much smaller than that on the total one. The other important aspect is that, being a mean-field model, it does not include possible variances in the polarized properties. So the polarized direction (the polarized angle) stays unchanged. The ratio of the maximum polarized intensity over the maximum total intensity goes from 0.7 for $\sigma = 0$ to 0.08 for $\sigma = \sqrt{10/3}$ ($\delta E = 10E$), while the total polarized fraction goes from 38 per cent for $\sigma = 0$ to 3 per cent for $\sigma = \sqrt{10/3}$. This shows how important future X-ray polarimetric measures could be.
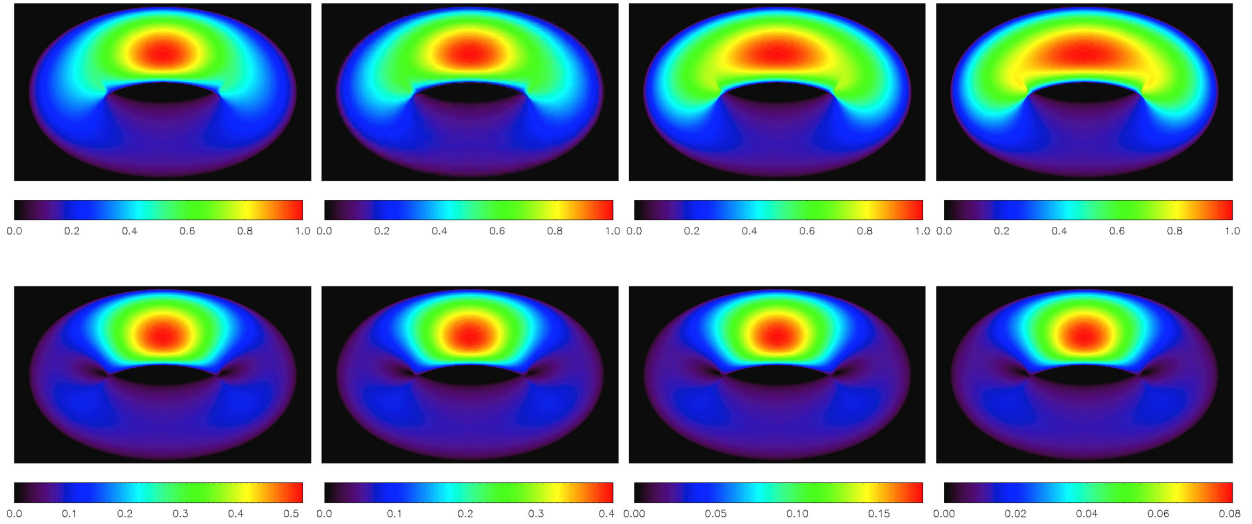
Figure 1. Upper panels: from left to right the total intensity normalized to its maximum value, for $\sigma = \sqrt{1/6}, \sqrt{1/3}, \sqrt{4/3}, \sqrt{10/3}$ (corresponding to ratios of energy in the fluctuating components over the one in the ordered toroidal component of 0.5,1,4,10, respectively). Lower panels: the same but for the polarized intensity, normalized to the maximum total intensity.
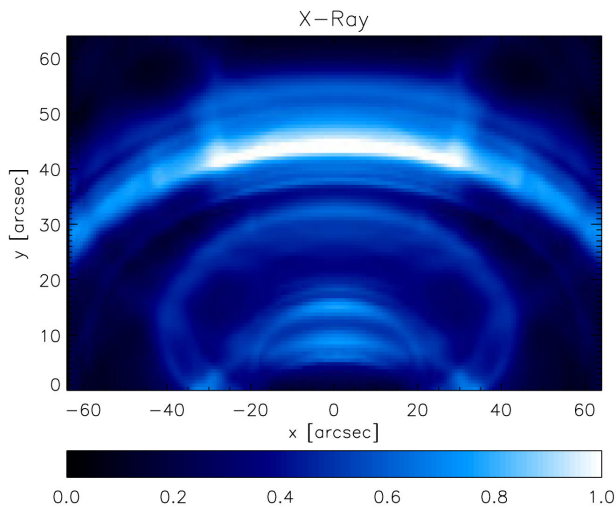

Figure 2. The upper hemisphere of the X-ray surface brightness map (1 keV) at $t = 950$ yr, in linear scale, as in Fig. 2 of Olmi et al. (2015), but for σ raising from 0.3 at $r = 0.6$ ly to 1 at $r = 1.25$ ly. Colour-scale normalized to the maximum.

However, some constraints can be drawn even now just by using available emission maps. The known polarized fraction of the Crab nebula in X-ray is $PF = 19.2 \pm 1$ (Weisskopf et al. 1978). Assuming it is mostly associated with the emission of the bright torus, this would suggest a value of σ in the range [0.6–0.8], corresponding to a value of the energy in the fluctuating components of the same order as the one in the ordered toroidal field.

As an example of application to more complex multidimensional models based on relativistic MHD simulations, in Fig. 2 we show how the simulated synchrotron map changes due to the inclusion of a small-scale fluctuating magnetic field. The model is the one described in Olmi et al. (2015) and targeted to the Crab nebula. For reference to the fully ordered case ($\sigma = 0$), one should take the map shown in fig. 2 of that same paper. Instead of just using a uniform value of σ for the fluctuating components of the magnetic field in the nebula, we have here opted to take a value increasing

with distance from $\sigma = 0.3$ at a radius from the centre $r = 0.6$ ly, to a maximum value $\sigma = 1$ at $r = 1.25$ ly. With this choice the inner wisp region is marginally affected, while fluctuations reach their maximum in correspondence with the location of the torus (see also the next section). The effects of this small-scale turbulent component are twofold: they raise the brightness of the sides of the various rings and arcs, as already discussed, and they also increase the relative brightness of those regions having a higher value of σ (the torus) with respect to the inner ones.

4 THE 'THIN TORUS' SEMI-ANALYTIC CASE

An even simpler approach can be attained if we consider the case of a very thin torus, i.e. $R_2/R_1 \to 0$ (and, as before, constant magnetic field and bulk velocity). In spite of its simplicity, the thin-torus model maintains most of the features of the more general case, with the advantage of allowing analytical formulae or series expansions that are useful for preliminary surveys of the parameters space. The points belonging to this torus are defined in the observer's coordinates system by

$$\boldsymbol{r} = (R_1 \cos i \cos \phi + Z \sin i, \; R_1 \sin \phi, \; -R_1 \cos \phi \sin i + z \cos i),$$
(20)

where i is the inclination angle of the symmetry axis with respect to the plane of the sky and where we also allow for a vertical displacement z of the plane of the torus along the symmetry axis. The first coordinate is the longitudinal coordinate, positive towards the observer, while the third one is aligned to the projection on the sky of the symmetry axis. If the points in the annulus have velocities with component $(\beta_R c, 0, \beta_z c)$ (in cylindrical coordinates), then the Doppler boosting factor (equation 5) reads

$$D(\phi) = \frac{\sqrt{1 - \beta_R^2 - \beta_z^2}}{1 - \beta_R \cos i \cos \phi - \beta_z \sin i},$$
(21)

while the transverse field in the emitters reference system (equation 7) is

$$|\boldsymbol{B}' \times \boldsymbol{n}'| = B' \sqrt{1 - D(\phi)^2 \cos i^2 \sin \phi^2},$$
(22)

where

$$B' = B\sqrt{1 - \beta_R^2 - \beta_z^2}. \tag{23}$$

The emissivity, as from equation (2), then reads

$$j = \left(C\nu^{-\alpha} B'^{\alpha+1}\right)\left(1 - D(\phi)^2 \cos i^2 \sin \phi^2\right)^{(\alpha+1)/2} D(\phi)^{\alpha+2}. \tag{24}$$

The power emitted per unit length of the transverse coordinate y (dI/dy) can be simply computed as $j(y)\Sigma(y)$, where Σ is the cross-section parallel to the symmetry axis and to the line of sight

$$\Sigma = \left(\pi R_2^2\right)/\sqrt{1 - \cos i^2 \sin \phi^2}. \tag{25}$$

The above quantities are expressed as explicit functions of ϕ, but profiles with respect to the variable y are easily obtained by the use of the relation $y = R_1 \sin\phi$ in equation (20).

Finally, in order to also derive the other Stokes parameters, we evaluate q_Y and q_Z (equation 12) as

$$q_Y = B\cos\phi - B(\beta_R \cos i + \beta_z \sin i \cos\phi), \tag{26}$$

$$q_Z = B\sin i \sin\phi - B\beta_z \sin\phi, \tag{27}$$

from which, using equation (13) the quantities $\cos 2\chi$ and $\sin 2\chi$ can be derived.

The most relevant aspect to investigate for the present discussion is how the intensity decreases moving away from the projected axis of symmetry, for the brighter (front) region of the torus. In the Appendix, we also discuss the intensity ratio between the two regions of the torus crossing the projected axis (front-to-back side brightness ratio), the geometry of the polarization swing (Bucciantini et al. 2005) due to the velocities of the emitters and other observables in the case of two symmetric rings (see also Section 5).

Let us expand the power per unit length to the second order in y/R_1, namely

$$\frac{dI(y)}{dy} \simeq \left.\frac{dI(y)}{dy}\right|_{y=0} \left(1 + \frac{S}{2}\frac{y^2}{R_1^2}\right). \tag{28}$$

The second derivative S is then evaluated as

$$S = \cos i^2 - \frac{(2+\alpha)\beta_R \cos i}{1 - \beta_R \cos i - \beta_z \sin i}$$
$$- \frac{(1+\alpha)\cos i^2(1 - \beta_R^2 - \beta_z^2)}{(1 + \beta_R \cos i - \beta_z \sin i)^2}. \tag{29}$$

In other terms, one can define a scalelength $y_S = R_1\sqrt{-1/S}$ for this intensity decrease.

The presence of a random magnetic field component does not affect the direction of polarization, but contributes both to the behaviour of the polarization fraction and to the pattern of the total intensity, the last one due to the fact that in the presence of a random magnetic field component synchrotron emission is less anisotropic.

We can derive a generalization of equation (29), valid for any value of σ

$$S(\sigma) = \left(\cos i^2 - \frac{(2+\alpha)\beta_R \cos i}{1 - \beta_R \cos i - \beta_z \sin i}\right) +$$
$$- \frac{(1+\alpha)\cos i^2\left(1 - \beta_R^2 - \beta_z^2\right)}{(1 + \beta_R \cos i - \beta_z \sin i)^2} G_{2,I}(\alpha, \sigma), \tag{30}$$

where

$$G_{2,I}(\alpha, \sigma) = \frac{{}_1F_1\left(\frac{1-\alpha}{2}, 2, -\frac{1}{2\sigma^2}\right)}{2\sigma^2 \, {}_1F_1\left(-\frac{1+\alpha}{2}, 1, -\frac{1}{2\sigma^2}\right)}. \tag{31}$$
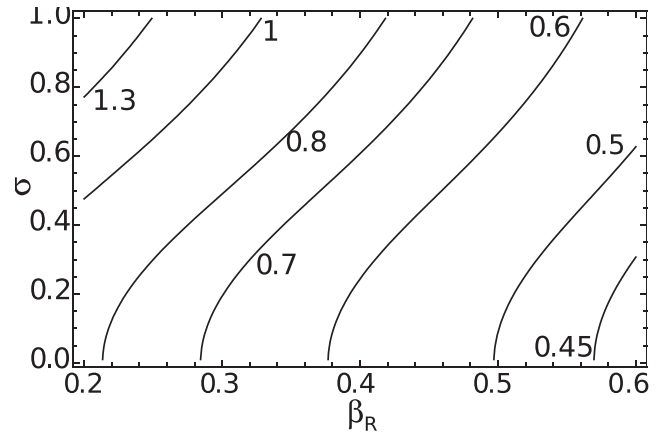

Figure 3. Value of the normalized $y_S/R_1 = 1/\sqrt{-S}$ brightness scale along a thin-ring (with respect to the symmetry axis) given by equation (30), as a function of β_R and σ. Labels of the contours are the values of y_S/R_1. The model is computed for $\beta_z = 0$, $i = 30°$ and $\alpha = 0.6$.

$G_{2,I}(\alpha, 0) = 1$, so that equation (29) is easily recovered for vanishing σ. The effect of fluctuations is to decrease the level of anisotropy of the emission and therefore to increase the estimated y_S scale, in this sense, the presence of fluctuations mimics a case with a lower value of v_R. Fig. 3 shows this behaviour.

For small σ values we propose the following approximation:

$$G_{2,I}(\alpha, \sigma)^{-1} = 1 + (1+\alpha)\sigma^2 + (1+\alpha)(1-\alpha)\sigma^4$$
$$+ 2(1+\alpha)(1-\alpha)^2\sigma^6$$
$$+ (1+\alpha)(1-\alpha)^2(7 - 5\alpha)\sigma^8 + \mathcal{O}(\sigma^{10}). \tag{32}$$

Its relative accuracy is, for instance, better than 1 per cent for $\sigma < 0.5$, in the range $0.5 < \alpha < 2.0$. In particular, it is exact in the case $\alpha = 1$, since $G_{2,I}(1, \sigma) = 1/(1 + 2\sigma^2)$.

5 APPLICATIONS

We apply here our model to the Crab and Vela PWNe. Following an approach similar to the one used by Ng & Romani (2004), we build a simulated synchrotron map to fit the three main components seen in X-rays: the torus, the inner ring and the jet. In order to obtain a reference image of the Crab nebula as shown in Fig. 2, we have aligned and combined 24 Chandra ACIS images of different epochs, ranging from 2012 to 2015, as retrieved from the Chandra Archive. Since each individual image presents a stripe corresponding to the chip gap, as well as the bright line aligned with the saturated pulsar image, before adding the images up we have masked these critical areas in all of them. Due to the different roll angles of the observations, the stripes in each image show a different orientation: therefore we successfully managed to add them up without leaving blind areas. Finally, a pixel-by-pixel correction has been applied to account for the difference in the effective exposure time due to the superposition of masked images having different orientations and offsets. In this way, the medium-large scale structure is very well reproduced; only the smaller scales are partially washed out, since the nebular structure is highly dynamical on those scales. Let us remark here that given the simplicity of the model we have adopted, we have not gone through a full-fledged data reduction. The data are simply used to derive rough constraints and not to place severe quantitative limits.

The torus and the inner ring are modelled as discussed in the previous section. The only difference is that now the volume emissivity
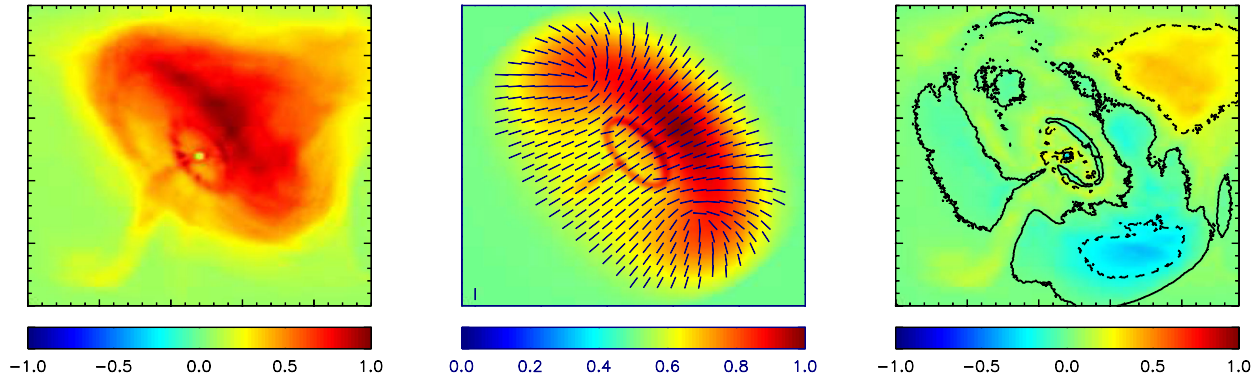
Figure 4. Left-hand panel: *Chandra* X-ray image of the Crab nebula. Intensity normalized to the maximum. Middle panel: our model of the Crab nebula. In the torus, we assume a flow velocity of $0.35c$ and $\sigma = 0.7$. Intensity normalized to the maximum with bars corresponding to the polarized direction. Right-hand panel: residuals obtained by subtracting the model from the data, normalized to the intensity maximum of the data. The solid line represents the zero level. The dashed lines represent the ± 20 per cent level.

is assumed to fall in a Gaussian way, as was done by Ng & Romani (2004), such that

$$K|B'|^{\alpha+1} \propto \exp\left[-\left((r\sin\theta - R_1)^2 + (r\cos\theta)^2\right)/2R_2^2\right]. \quad (33)$$

The symmetry axis is inclined by $27°$ on the plane of the sky and $55°$ with respect to the north (Weisskopf et al. 2000). The main torus has $R_1/R_2 = 3.45$ while for the inner ring we took $R_1/R_2 = 10$. The same spectral index $\alpha = 0.6$ was used for both (Mori et al. 2004). Optical polarization suggests that in the inner ring the ordered component of the magnetic field is toroidal. There is no information on the structure of the magnetic field in the torus or jet, even if large-scale optical polarization maps are compatible with a toroidal geometry. This is consistent with simulations (and symmetry arguments) suggesting that the field should be mostly azimuthal in the torus. On the other hand, the jet is seen to be turbulent and time varying. A model for the X-ray luminosity of the inner ring was already presented in Schweizer et al. (2013), where it was shown that it is possible to reproduce it using a typical boost speed of $\sim 0.6c \pm 0.1c$. No strong constraints can be placed on the ratio of disordered versus ordered field in the inner ring mostly because of the low photon counts and due to the presence of bright time-varying non-axisymmetric features. Thus, in the toy model we set for the inner ring $\sigma = 0.3$ in order to give a polarized fraction for the ring alone of ~ 40 per cent as seen in optical (suggesting that already close to the termination shock about one-third of the magnetic energy is in the small-scale fluctuating part). On the other hand, the jet, being a faint feature, can be reproduced with a fully turbulent field as well as a fully ordered one. Here we decide to include it (by considering the case of a fully turbulent field) only to reduce the residuals on the axis. Our best-fitting model for the Crab torus requires a typical boosting speed of the order of $\simeq 0.35c \pm 0.05c$ and a level of fluctuating magnetic field $\sigma \simeq 0.6-0.9$. With these values we get a total polarized fraction of $\sim (17 \pm 2)$ per cent in agreement with observations. The value of σ cannot be raised above unity, otherwise the total polarized fraction becomes smaller than 15 per cent, underestimating the data.

In Fig. 4, we show our reference image for the Crab nebula, our best-fitting model, and the residuals between the data and the model. In Fig. 5, we show the residuals in the fully ordered case $\sigma = 0$, where in order to get brighter sides of the torus we had to lower the boosting speed to the possible smallest value $(0.25-0.3)c$. We cannot lower it further. However, looking carefully at the residuals, one can see that even if we are able to get the correct front-to-back side
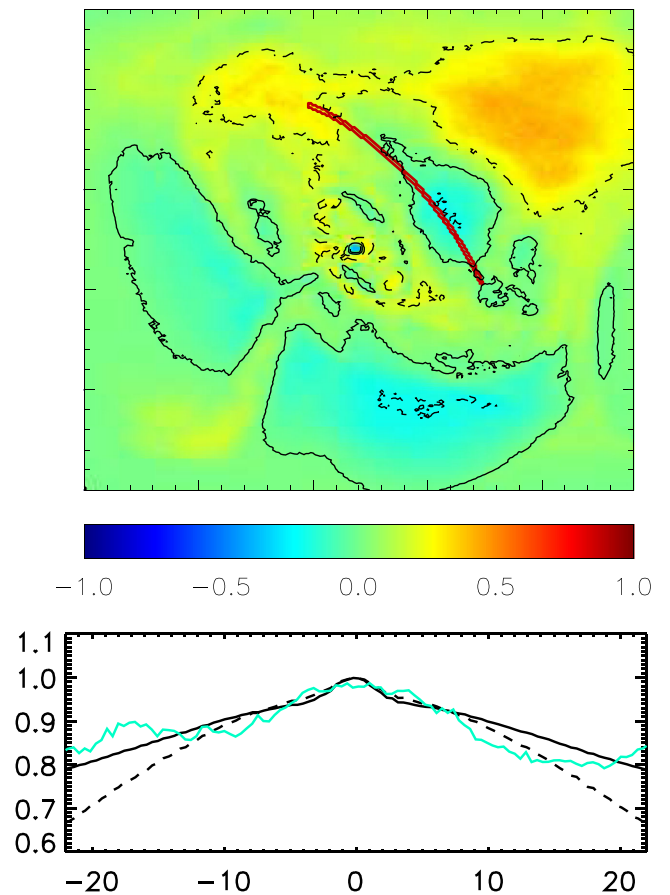

Figure 5. Upper panel: map of the residuals for the Crab nebula defined as for Fig. 4, but with respect to a model with fully ordered toroidal magnetic field. The flow velocity is set to $0.3c$ in order to match the front to back brightens difference, while in the torus $\sigma = 0$. The solid line represents the zero level. The dashed line represents the ± 20 per cent level. Lower panel: comparison of the surface brightness in the region defined by the red arc in the upper panel (cyan line) to the model with $\sigma = 0.7$ (solid line) and to the one with $\sigma = 0$ (dashed line). The curves have been re-scaled to match the maximum of the intensity. The x-axis is in arcsec from the peak. The y-axis is in arbitrary units normalized to the peak.

brightness difference, this model tends to under-predict the front-to-sides one, on both sides of the torus. To make this difference clearer, in the bottom panel of Fig. 5, we compare the X-ray surface brightness of the torus, sampled along the arc shown in the upper panel of the same figure, to our two models: the one with a fluctuating small scale field with $\sigma = 0.7$ and the one with a fully ordered field with $\sigma = 0$. It is evident that both models give a reasonable fit in the central (on axis) part of the torus within ± 10 arcsec from the peak, where they can hardly be distinguished. However, the wings of the torus beyond ± 15 arcsec are slightly underpredicted by the fully ordered case. On top of this the integrated polarized fraction for the fully ordered case is estimated to be ~ 30 per cent. This is much higher than the measured value of 19 per cent and, given that the torus is by far the brightest feature in X-ray, it is unlikely that the low surface brightness diffuse X-ray emission could provide enough unpolarized radiation to compensate.

As shown in Fig. 4, in the region of the ring and the torus, our best-fitting model provides residuals below 15 per cent. Given, however, the presence of a non-uniform and diffused X-ray nebular emission, the fact that the torus itself is brighter on one side, the fact that the ring is not exactly centred on the pulsar and that there are non-axisymmetric features like the north-west spur, it is obvious that our axisymmetric model cannot provide an accurate fit. But in its simplicity it already indicates that the brightness profile of the torus points towards a possibly large level of turbulence (about half of the magnetic energy should be in the small-scale fluctuating part).

We have repeated a similar analysis for the Vela PWN. To get a reference image, we have followed a procedure similar to that already described for the Crab nebula, combining 19 Chandra ACIS images relative to the period from year 2001 to 2010. Since the relevant areas in individual images now are not affected by the chip gap, we have simplified the masking procedure with respect to the previous case. As shown in Fig. 6, the X-ray nebula is characterized by two tori and a small jet. Due to the presence of a large and diffuse X-ray emission, and to the brightness of the pulsar, we have limited our investigation to the brightness profile of the two tori, without attempting a global fit of the emission map. In the upper panel of Fig. 6, we show the regions of the tori where we have extracted the brightness profiles shown in the bottom panel. We model the tori, as was done for the Crab nebula, using the Gaussian profile of equation (33), with $R_2/R_1 = 5.9$ and 5.3 for the outer and inner torus, respectively. The symmetry axis is inclined by $33°$ on the plane of the sky and $130°$ with respect to the north. A jet (and counter-jet) was also introduced with radial velocity equal to $0.7c$, in order to reproduce the brightness peak observed on axis in the outer torus. The spectral index is fixed at $\alpha = 0.3$ (Kargaltsev & Pavlov 2004). The brightness difference between the front side (on axis) of the tori and the back side constrains the radial flow speed to be higher than $0.35c$. In the bottom panel of Fig. 6, the brightness profile of the tori is compared to a fully ordered case $\sigma = 0$ with radial velocity $0.35c$ and to a case with $\sigma = 1$ and radial velocity $\approx 0.5c$. Again it is evident that the two models begin to differ substantially beyond 10 arcsec from the axis. For the inner torus the difference between the two cases is small. This happens because the sides of the inner torus are superimposed along the line of sight to the back part of the outer torus so that their brightness does not decline as fast. On the other hand, the model with a fully ordered magnetic field underpredicts the brightness of the sides of the outer torus. A better agreement is achieved by the model with $\sigma = 1$. However, we remark here that the presence of a large diffuse X-ray emission does not allow us to perform a satisfactory global fitting of the emission map using
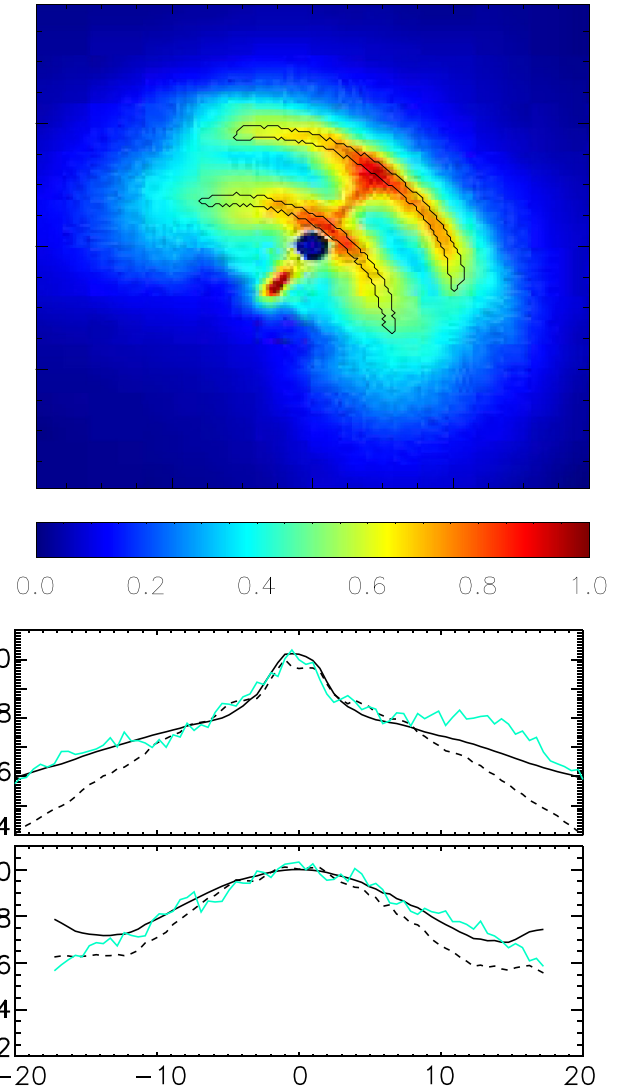

Figure 6. Upper panel: brightness map of the Vela PWN, normalized to the maximum. Axes in arcsecs. The central region containing the pulsar has been excised. The two arcs represent the region of the inner torus and outer torus whence the brightness profile was extracted. Lower panel: comparison of the surface brightness in the outer torus (above) and inner torus (below), measured in the arcs shown in the upper panel, to the model with $\sigma = 1$ (solid line) and to the one with $\sigma = 0$ (dashed line). The x-axis is in arcsec from the peak. The y-axis is in arbitrary units normalized to the peak.

a simple prescription as equation (33). We can use our models to provide upper limits to the total integrated polarized fraction. For $\sigma = 0$, we expect $PF \leq 23$ per cent, while for $\sigma = 1$ we find that the polarized fraction should be ≤ 6 per cent. Only future polarimetric measures could help us to identify the correct regime.

6 CONCLUSIONS

Driven by the increasing evidence pointing towards the presence of a possibly large magnetic turbulence in PWNe and the interest in future X-ray polarimetric observations, we have developed here a simple formalism to simulate the effect of a small-scale fluctuating magnetic field on the emission properties of PWNe, and potentially of other synchrotron emitting sources, and we have shown how to build emission maps to be compared with observations. We

find that in general there is a degeneracy between the effects of a turbulent component and the Doppler boosting. Both regulate how the brightness changes along rings and tori: the front-to-sides brightness difference can be lowered assuming either a lower flow speed or a higher level of turbulence. We showed however that this degeneracy can be partially broken looking at the front-to-back brightness difference, which depends only on Doppler boosting. We have applied our analysis to the Crab and Vela PWNe, showing that models with a sizable fraction of magnetic energy into a small-scale turbulent component seem to provide a better fit for the tori. In the case of the Crab nebula, where integrated polarimetric measures are available, our turbulent model gives a consistent estimate of the polarized fraction. For the Vela PWN we provide only rough estimates of upper limits for future observations. Our results show that, while evidence for a turbulent component can already be guessed from emission maps, future X-ray polarimetric measures, even of just integrated polarized fraction, will be crucial to set stronger constraints. This could also help to clarify if the observed morphological difference in X-ray PWNe is possibly related to different levels of turbulence.

REFERENCES

Aumont J. et al., 2010, A&A, 514, A70
Bandiera R., Petruk O., 2016, MNRAS, 459, 178
Bucciantini N., 2010, in Bellazzini R., Costa E., Matt G., Tagliaferri G., eds, Polarization of Pulsar Wind Nebulae. Cambridge Univ. Press, Cambridge, p. 195
Bucciantini N., del Zanna L., Amato E., Volpi D., 2005, A&A, 443, 519
Bühler R., Blandford R., 2014, Rep. Prog. Phys., 77, 066901
Camus N. F., Komissarov S. S., Bucciantini N., Hughes P. A., 2009, MNRAS, 400, 1241
Conway R. G., 1971, in Davies R. D., Graham-Smith F., eds, Proc. IAU Symp. 46, The Crab Nebula. Reidel, Dordrecht, p. 292
Del Zanna L., Amato E., Bucciantini N., 2004, A&A, 421, 1063
Del Zanna L., Volpi D., Amato E., Bucciantini N., 2006, A&A, 453, 621
DeLaney T., Gaensler B. M., Arons J., Pivovaroff M. J., 2006, ApJ, 640, 929
Ferguson D. C., 1973, BAAS, 5, 425
Gaensler B. M., Slane P. O., 2006, ARA&A, 44, 17
Gaensler B. M., Arons J., Kaspi V. M., Pivovaroff M. J., Kawai N., Tamura K., 2002, ApJ, 569, 878
Helfand D. J., Gotthelf E. V., Halpern J. P., 2001, ApJ, 556, 380
Hester J. J., 2008, ARA&A, 46, 127
Kargaltsev O., Pavlov G., 2004, in Camilo F., Gaensler B. M., eds, Proc. IAU Symp. 218, Young Neutron Stars and Their Environments. Astron. Soc. Pac., San Francisco p. 195
Komissarov S. S., Lyubarsky Y. E., 2003, MNRAS, 344, L93
Komissarov S. S., Lyubarsky Y. E., 2004, MNRAS, 349, 779
Marubini T. E., Sefako R. R., Venter C., de Jager O. C., 2015, in van Rensburg J. J., ed, Proc. SAIP2012: the 57th Annual Conference of the South African Institute of Physics, p. 340
Moran P., Shearer A., Mignani R. P., Słowikowska A., De Luca A., Gouiffès C., Laurent P., 2013, MNRAS, 433, 2564
Moran P., Mignani R. P., Shearer A., 2014, MNRAS, 445, 835
Mori K., Burrows D. N., Hester J. J., Pavlov G. G., Shibata S., Tsunemi H., 2004, ApJ, 609, 186
Ng C.-Y., Romani R. W., 2004, ApJ, 601, 479
Olmi B., Del Zanna L., Amato E., Bandiera R., Bucciantini N., 2014, MNRAS, 438, 1518
Olmi B., Del Zanna L., Amato E., Bucciantini N., 2015, MNRAS, 449, 3149
Olmi B., Del Zanna L., Amato E., Bucciantini N., Mignone A., 2016, J. Plasma Phys., 82, 635820601
Pavlov G. G., Kargaltsev O. Y., Sanwal D., Garmire G. P., 2001, ApJ, 554, L189
Porth O., Komissarov S. S., Keppens R., 2014, MNRAS, 438, 278
Schweizer T., Bucciantini N., Idec W., Nilsson K., Tennant A., Weisskopf M. C., Zanin R., 2013, MNRAS, 433, 3325
Soffitta P. et al., 2013, Exp. Astron., 36, 523
Tanaka S., Asano K., 2016, Supernova Remnants: An Odyssey in Space after Stellar Death, p. 57
Tang X., Chevalier R. A., 2012, ApJ, 752, 83
Uzdensky D. A., Cerutti B., Begelman M. C., 2011, ApJ, 737, L40
Velusamy T., 1985, MNRAS, 212, 359
Volpi D., Del Zanna L., Amato E., Bucciantini N., 2007, Mem. Soc. Astron. Ital., 78, 662
Weisskopf M. C., Silver E. H., Kestenbaum H. L., Long K. S., Novick R., 1978, ApJ, 220, L117
Weisskopf M. C. et al., 2000, ApJ, 536, L81
Weisskopf M. C. et al., 2016, in den Herder J.-W. A., Takahashi T., Bautz M., eds, Proc. SPIE Conf. Ser. Vol. 9905, Space Telescopes and Instrumentation 2016: Ultraviolet to Gamma Ray. SPIE, Bellingham, p. 990517
Zrake J., Arons J., 2016, preprint (arXiv:e-prints)

APPENDIX: THIN-RING

We illustrate here how to derive other observable quantities of interest for a thin-ring (or a pair of symmetric rings), as a function of inclination, bulk velocity and level of turbulence.

Following what was done in Section 4, we begin with the ratio of the intensity of the front side ($\phi = 0$) to that on the back side ($\phi = \pi$), which is independent of the value σ

$$\frac{dI(y)}{dy}\bigg|_{\phi=0} \bigg/ \frac{dI(y)}{dy}\bigg|_{\phi=\pi} = \left(\frac{1 + \beta_R \cos i - \beta_z \sin i}{1 - \beta_R \cos i - \beta_z \sin i}\right)^{2+\alpha}. \tag{A1}$$

Another parameter accessible through polarization measures is the direction of polarization angle χ (with respect to the horizontal axis), that in the absence of motion is simply given by

$$\sin \chi = N \sin i \sin \phi, \qquad \cos \chi = N \cos \phi, \tag{A2}$$

with a normalization factor such that $N^2 = (\sin^2\phi \sin^2 i + \cos^2\phi)^{-1}$ (the quantity N can have either a positive or negative sign, corresponding to the fact that the polarization angle is defined modulus π). The above formulae simply reflect the geometrical effect of the inclined view. Instead, in the presence of motions this orientation is distorted by relativistic effects (polarization swing) and the equations give

$$\sin \chi = N(\sin i - \beta_z) \sin \phi, \tag{A3}$$

$$\cos \chi = N(\cos \phi - \beta_R \cos i - \beta_z \sin i \cos \phi). \tag{A4}$$

It is interesting to derive the quantity $\delta\chi$, namely the deviation of the polarization direction from the purely geometrical case (zero velocities). Using the above relations and the formula for the tangent of a sum of angles, one derives

$$\tan(\delta\chi) = \frac{\sin \phi \, \cos i \, (\beta_R \sin i - \beta_z \cos i \, \cos \phi)}{(\cos^2\phi + \sin^2\phi \, \sin^2 i) - (\beta_R \cos \phi \, \cos i + \beta_z \sin i)}, \tag{A5}$$
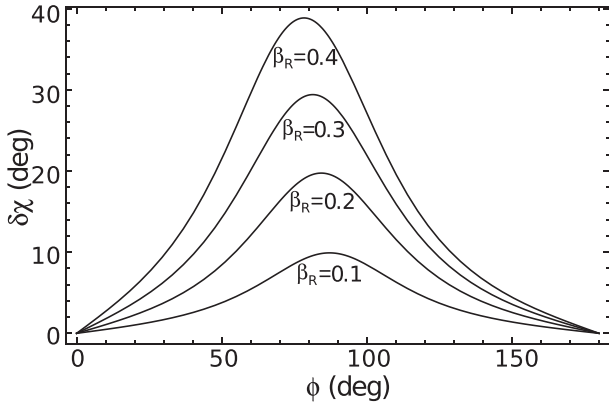
Figure A1. Trend of the polarization angle swing $\delta\chi$ as definded in equation (A5), for different values of the velocity β_R in the case $\beta_z = 0$, $i = 30°$ and $\alpha = 0.6$.
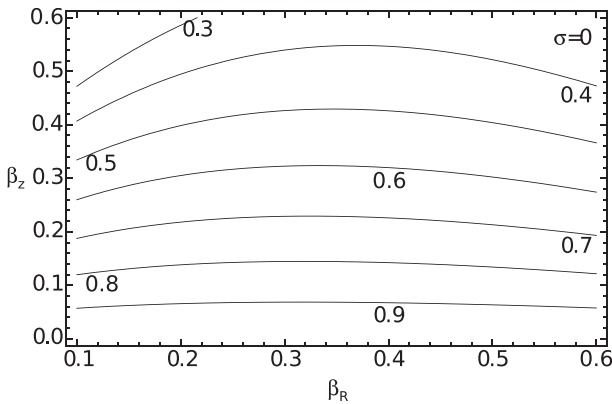

Figure A2. Trend of the $y_{S,+}/y_{S,-}$ ratio for two rings symmetric with respect to the equator, as a function of β_z and β_R, for $i = 30°$ and $\alpha = 0.6$.

with a positive $\delta\chi$ meaning a wider angle, with respect to the purely geometrical case, from the direction of the mid-point of the brighter front side. At least in principle, following the behaviour of $\delta\chi$, one could fit independently β_R and β_z (which could be different from zero for a ring with a vertical offset from the equator). In Fig. A1 we show this trend.

Non-vanishing values of β_z are expected in the case of a pair of rings, like for instance in the case of Vela. It is then possible to estimate the value of β_z by comparing the y_S scalelength of the two tori. To keep the system symmetric, let us assume equal values of β_z in the two rings, but with opposite signs; in this case, Fig. A2

shows that the ratio $y_{S,+}/y_{S,-}$ is strongly dependent on β_z while it is almost independent of β_R and therefore possibly represents a good diagnostic for β_z. It can be shown that this quantity is also almost independent of σ.

Finally, let us discuss the effect of fluctuations on the polarization fraction (*PF*). By adopting the same kind of procedure as before, namely expanding to the second order in y and then approximating the coefficients in the limit of small values of σ, we get:

$$PF(y) \simeq \frac{\alpha+1}{\alpha+5/3} \left(G_{0,PF}(\alpha, \sigma) + \frac{S_P}{2}\frac{y^2}{R_1^2} \right), \tag{A6}$$

where

$$G_{0,PF}(\alpha, \sigma) = \frac{(3+\alpha)\,_1F_1\left(\frac{1-\alpha}{2}, 3, -\frac{1}{2\sigma^2}\right)}{8\sigma^2\,_1F_1\left(-\frac{1-\alpha}{2}, 1, -\frac{1}{2\sigma^2}\right)}, \tag{A7}$$

whose inverse, for small σ values, is well approximated by

$$G_{0,PF}(\alpha,\sigma)^{-1} = 1 + 2\sigma^2 + 2(1-\alpha)\sigma^4 - 4\alpha(1-\alpha)\sigma^6 + \\ - 2(1-\alpha)^2(3+5\alpha)\sigma^8 + \mathcal{O}(\sigma^{10}). \tag{A8}$$

Finally, the quantity S_P evaluates

$$S_P(\sigma) = -\frac{2\cos^2 i\,\left(1 - \beta_R^2 - \beta_z^2\right)}{(1 - \beta_R\cos i - \beta_z\sin i)^2}\left(1 - G_{2,PF}(\alpha, \sigma)\right), \tag{A9}$$

where

$$G_{2,PF}(\alpha, \sigma) = \frac{(1+\alpha)\,_1F_1\left(\frac{1-\alpha}{2}, 2, -\frac{1}{4\sigma^2}\right)}{4\sigma^2\,_1F_1\left(-\frac{1+\alpha}{2}, 1, -\frac{1}{2\sigma^2}\right)} \\ + \frac{(1-\alpha)\,_1F_1\left(\frac{3-\alpha}{2}, 4, -\frac{1}{2\sigma^2}\right)}{12\sigma^2\,_1F_1\left(\frac{1-\alpha}{2}, 3, -\frac{1}{2\sigma^2}\right)}. \tag{A10}$$

It can be shown that $G_{2,PF}(\alpha, \sigma)$ tends to 1 for vanishing σ, namely the polarization fraction is a constant for a completely ordered field. The power series approximation of this quantity with σ is

$$G_{2,PF}(\alpha, \sigma)^{-1} = 1 + 2\sigma^2 + 4(1-\alpha)\sigma^4 + \\ + 4(1-\alpha)(1-3\alpha)\sigma^6 + \\ - 8(1-\alpha)(2+5\alpha - 5\alpha^2)\sigma^8 + \mathcal{O}(\sigma^{10}). \tag{A11}$$

Clearly this property depends strongly on the assumption of a thin-ring. For thick tori (see the main text) depolarization effects due to integration along the line of sight play, instead a more relevant role.

This paper has been typeset from a TEX/LATEX file prepared by the author.